

Highlights

Modeling the Impact of Iron Defect Variability on Silicon Solar Cell Performance Across Different Scenarios

Oleg Olikh, Oleksii Zavhorodnii

- 1
- 2
- 3

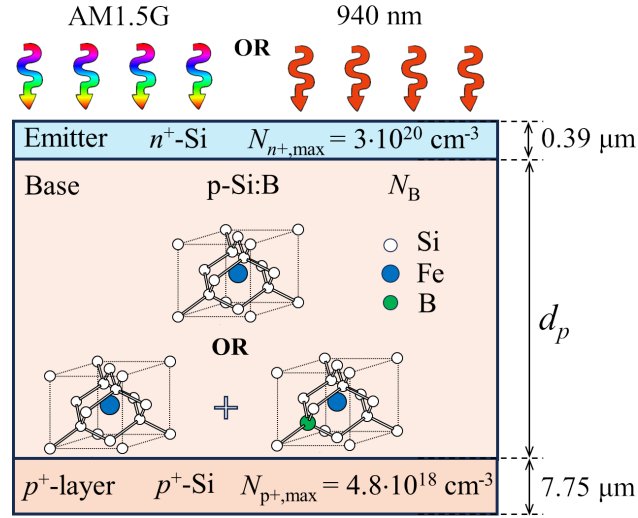


Figure 1: Schematic diagram of analyzed solar cells.

based on changes in the ideality factor [27, 28] or open-circuit voltage [17]. However, developing such approaches requires evaluating how a particular parameter changes when iron-containing pairs dissolve and determining whether it can estimate the iron concentration N_{Fe} . For example, the most evident conditions for utilizing a specific parameter include its change due to the transformation $Fe_i B_{Si} \rightarrow Fe_i + B_{Si}$, at least by 10 %, along with a monotonic dependence of these changes on N_{Fe} .

This paper intends to determine the variations of I_{SC} , V_{OC} , η , and FF resulting from the decay of iron-containing pairs in boron-doped silicon solar cells. Previous similar calculations have been conducted [29, 16, 10], but the results presented typically pertain only to certain temperatures, illumination levels (often AM1.5), and solar cells with specific parameters. In this study, we performed calculations over a sufficiently wide temperature range (290-340 K) and for solar cells with varying base thickness (180-380 μm) and doping levels (boron concentration in the base ranging from 10^{15} to 10^{17} cm^{-3}). The results obtained allow us to assess the feasibility and potential of using the main photovoltaic parameters of specific solar cells to estimate the N_{Fe} value across a range of temperatures, including conditions similar to those encountered in typical SSC applications. Furthermore, investigations have explored changes in photoelectric performance under not only solar illumination (AM1.5G) but also low-intensity monochromatic light (wavelength of 940 nm, intensities of 5 W/m² and 10 W/m²). In the first case, while it is customary to adhere to standard conditions, it's essential to consider that illumination at 1000 W/m² can lead to the decay of $Fe_i B_s$ complexes [30]. Therefore, measurements for cases requiring the presence of undissociated pairs in silicon must meet specific constraints. On the other hand, intentionally chosen monochromatic illumination penetrates the emitter with negligible losses and does not reach the rear side. In this context, the photoelectric parameters show remarkable sensitivity to recombination processes occurring within the solar cell base and to iron concentration in this region. Finally, in our calculations, we attempted to use the latest literature data concerning the exact values of silicon parameters, including light absorption values [31] and coefficients characterizing intrinsic recombination [32, 33].

2. Research Methodology

2.1. Simulation Details

The study involved simulation I - V curves of SSCs with an $n^+ - p - p^+$ structure, as illustrated in Fig. 1. A back surface field (p⁺-layer) is a notable feature observed in both Al-BSF cells (full area), which are gradually losing relevance, and PERC cells (locally), which are the most widely used in mass production. The structures with a base uniformly doped with boron were under consideration. The doping concentration N_B , and the base thickness d_p were varied during the modeling process, as detailed in Table 1. The emitter and p⁺-layer were considered to be unevenly doped. The concentration profiles of the dopants, their maximum values ($N_{p^+,max}$ and $N_{n^+,max}$), and layer thicknesses (see Fig. 1) were selected according to Fell et al. [34].

Table 1

Parameters varied during the simulation

Parameter	Range of values
d_p (μm)	180 – 380
N_B (cm^{-3})	$10^{15} - 10^{17}$
N_{Fe} (cm^{-3})	$10^{10} - 10^{14}$
T (K)	290 – 340
Illumination	AM1.5G, 1000 W/m ² ; 940 nm, 5 W/m ² ; 940 nm, 10 W/m ²

The simulation was conducted using the SCAPS 3.3.11 code [35]. SCAPS-1D software, developed by the University of Gent, is founded on theoretical computations that involve solving Poisson's equation, continuity equations for holes and electrons, and drift-diffusion at each position within the solar cell, considering the boundary conditions. Despite its one-dimensional modeling approach, SCAPS is extensively used for modeling various types of solar cells [36, 37, 38, 39] in general and for investigating the effects of defects on their performance [40, 41, 42] in particular.

As can be seen from Table 1, calculations spanned a broad range of temperatures and base doping levels. Therefore, to improve the accuracy of the calculations when inputting the initial parameters into SCAPS, temperature and concentration (where applicable) dependencies of the following silicon parameters were taken into account:

- bandgap according to Passler [43];
- doping induced bandgap narrowing according to Yan & Cuevas [44];
- effective density of states at conduction and valence band and intrinsic carrier concentration according to Couderc et al. [45];
- thermal carrier velocities according to Green [46];
- free carrier effective masses according to O'Mara et al. [47];
- carrier mobilities according to Klaassen's theory [48];

The values of surface recombination coefficients were considered equal to the thermal velocities of carriers [34]. The calculations addressed recombination processes within the structural volume, incorporating both intrinsic recombination and Shockley-Read-Hall recombination at iron-related defects. In the first case, processes of band-to-band radiation recombination were considered (where the calculation of the corresponding coefficient included the fraction of radiatively emitted photons reabsorbed via band-to-band processes according to Niewelt et al.[32]) and Auger recombination (where the coefficients considered the effect of Coulomb enhancement [33] and temperature dependence [49]).

When accounting for the influence of iron impurities, we considered that Fe atoms were uniformly distributed within the base and p^+ -layer with a total concentration of N_{Fe} (see Table 1). Two cases were under consideration:

Case 1. The concentration of interstitial iron defects $[Fe_i] = N_{Fe}$ at each position throughout the solar cell, with no pairs present $[Fe_iB_s] = 0$. This case corresponds to the state of the structure immediately after intense illumination, for example.

Case 2. Iron atoms predominantly form pairs with acceptors, $[Fe_iB_s] \gg [Fe_i]$, but the exact concentration ratio depends on the position of the Fermi level and temperature [50, 51] and varies from point to point within the solar cell. Further details about calculation of the concentration profiles of Fe_iB_s and Fe_i are provided in [28, 27]. This case corresponds to prolonged storage of the structure in darkness or under conditions of low-intensity ($< 0.01 \text{ J cm}^{-2}$ [30]) illumination.

During the calculations, it was assumed that Fe_i forms a single donor level, while the Fe_iB_s pair has a trigonal configuration and acts as an amphoteric defect. We obtained defect parameters (including level positions within the bandgap and electron and hole capture cross-sections) from relevant studies [52, 53].

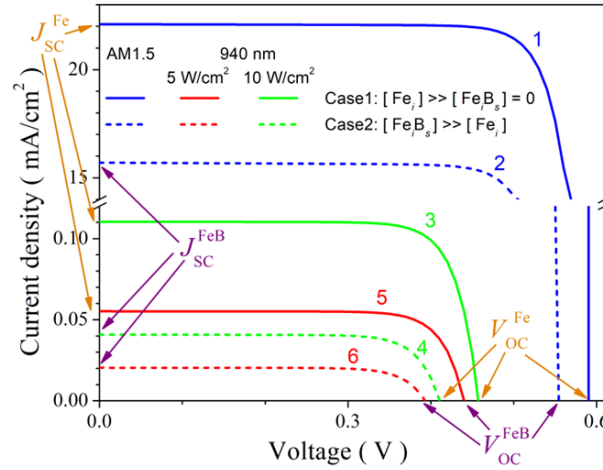


Figure 2: Typical IV characteristics, calculated for structure with $d_p = 180 \mu\text{m}$, $N_B = 10^{17} \text{ cm}^{-3}$, $N_{Fe} = 10^{14} \text{ cm}^{-3}$ at $T = 290 \text{ K}$. Illumination: AM1.5 (curves 1, 2), 940 nm 10 Wcm^{-2} (3, 4) and 940 nm 5 Wcm^{-2} (5, 6). Solid and dotted lines correspond to Case 1 and Case 2, respectively.

As previously mentioned, the solar cell behavior was simulated under different illumination conditions, including solar light (AM1.5G) and monochromatic light (wavelength 940 nm, intensity of $W_{\text{ill}} = 5 \text{ Wm}^{-2}$ or 10 Wm^{-2}) — see Table 1. The calculations incorporated the light absorption values in silicon based on Green's study [31].

The I - V characteristics were simulated for both Case 1 and Case 2 (see Fig. 2), and from each curve, the short-circuit current, open-circuit voltage, efficiency, and fill factor were determined. Assessing the influence of iron defect variability relied on the relative changes in each photovoltaic conversion parameter:

$$\varepsilon A = \frac{A^{\text{FeB}} - A^{\text{Fe}}}{A^{\text{FeB}}} \times 100\%, \quad (1)$$

where A represents one of the parameters (I_{SC} , V_{OC} , η , and FF), superscript “FeB” corresponds to the parameter value for coexistence of Fe_i and Fe_iB_s (Case 2), superscript “Fe” is related to the decay of all pairs (Case 1).

Impact of change of iron defects was investigated as a function of temperature from 290 K to 340 K, base depth from $180 \mu\text{m}$ to $380 \mu\text{m}$, base doping level from 10^{15} cm^{-3} to 10^{17} cm^{-3} , and total impurity iron atom concentration from 10^{10} cm^{-3} to 10^{14} cm^{-3} . For each illumination scenario, calculations were carried out with 11 different temperature values and 5 base depth values, evenly distributed within the specified ranges. The concentration values were distributed equally on a logarithmic scale with 4 (N_B case) and 6 (N_{Fe} case) steps per decade. As a result, for the AM1.5 illumination scenario, for instance, 24750 I - V characteristics were simulated. An exception occurred with monochromatic illumination at $W_{\text{ill}} = 10 \text{ Wm}^{-2}$, where we used only two d_p values.

2.2. Experimental Details

To evaluate the validity of the simulated results, we also conducted experimental studies on the effect of changing the state of iron-related defects on the photoelectric parameters of silicon solar cells.

The n^+ - p - p^+ -Si samples were used in the experiment. The structure was fabricated from a $380 \mu\text{m}$ thick p -type boron-doped Czochralski silicon (100) wafer with doping level $N_B = 1.36 \times 10^{15} \text{ cm}^{-3}$. The n^+ emitter with a sheet resistance of about $20\text{--}30 \Omega/\square$ and thickness of $0.7 \mu\text{m}$ was formed by phosphorus diffusion. The anti-recombination isotype barrier was created by using a p^+ layer ($10\text{--}20 \Omega/\square$) formed by boron diffusion. On the front surface, SiO_2 (40 nm) and Si_3N_4 (30 nm) films were formed as antireflective and passivating layers, respectively. The solid and grid Al contacts were formed by magnetron sputtering on the back and front surfaces, respectively.

The I - V characteristics were measured using a Keithley 2450 source meter and low-intensity monochromatic light source (light-emitting diode SN-HPIR940nm-1W with light wavelength 940 nm and intensity of about $W_{\text{ill}} = 5 \text{ Wm}^{-2}$).

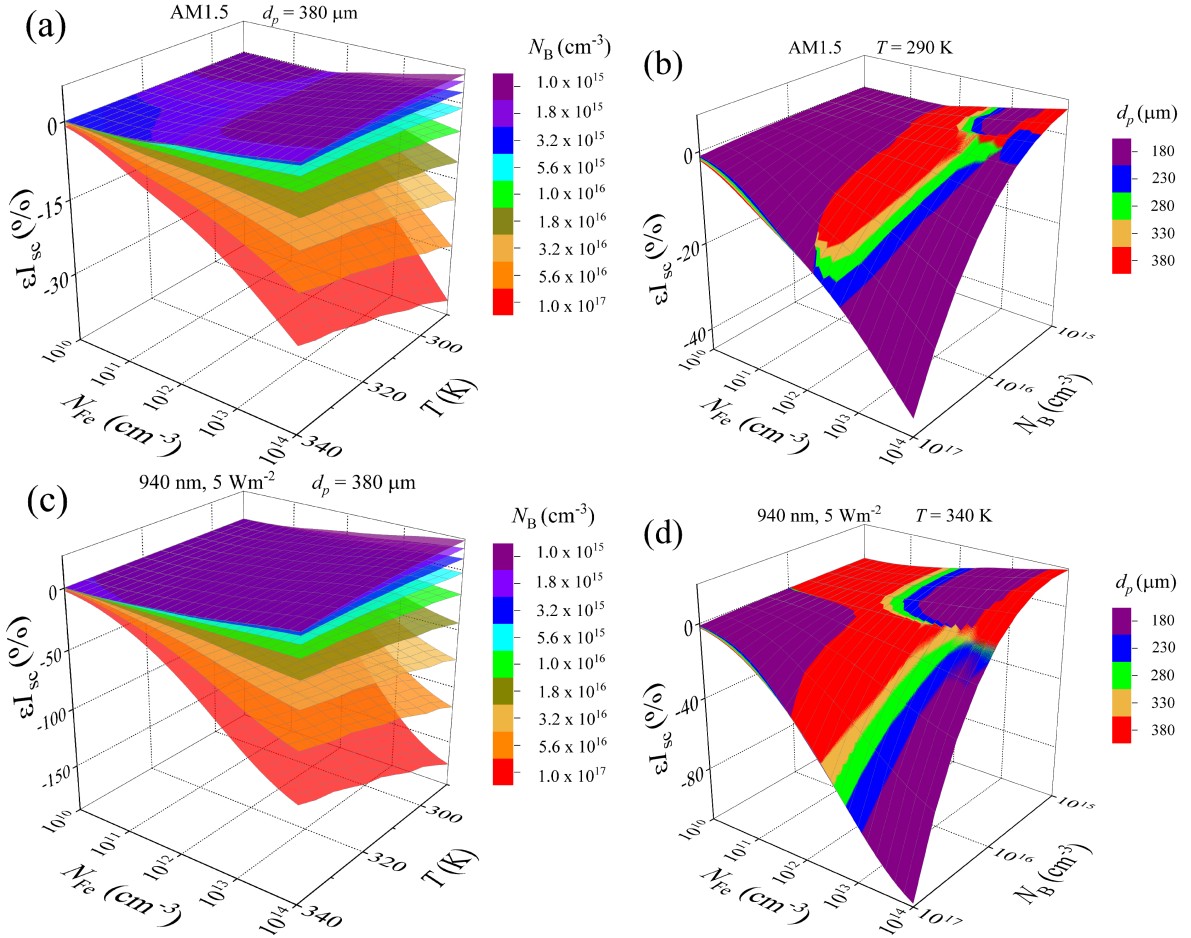


Figure 3: Dependencies of relative changes of short-circuit current on iron concentration and temperature (panels a and c) or doping level (b, d). Illumination: AM1.5 (a, b), 940 nm $5 Wm^{-2}$ (c, d). T , K: 290 (b), 340 (d). Different surfaces correspond to different doping levels (a, c) and base depths (b, d).

For different samples, the iron concentration ranged from 2×10^{11} to $4 \times 10^{13} cm^{-3}$. The values of N_{Fe} were determined using a methodology [54, 25], based on fitting the kinetics of short-circuit current. The decay of Fe_iB_s pairs was realized using intensive ($7000 W/m^2$) halogen lamp illumination.

The measurements were carried over the temperature range of 300–340 K. The sample temperature was driven by a thermoelectric cooler controlled by an STS-21 sensor and maintained constant by a PID algorithm embedded in the software that serves the experimental setup.

3. Results and Discussion

3.1. Short-circuit current

[55, 56]

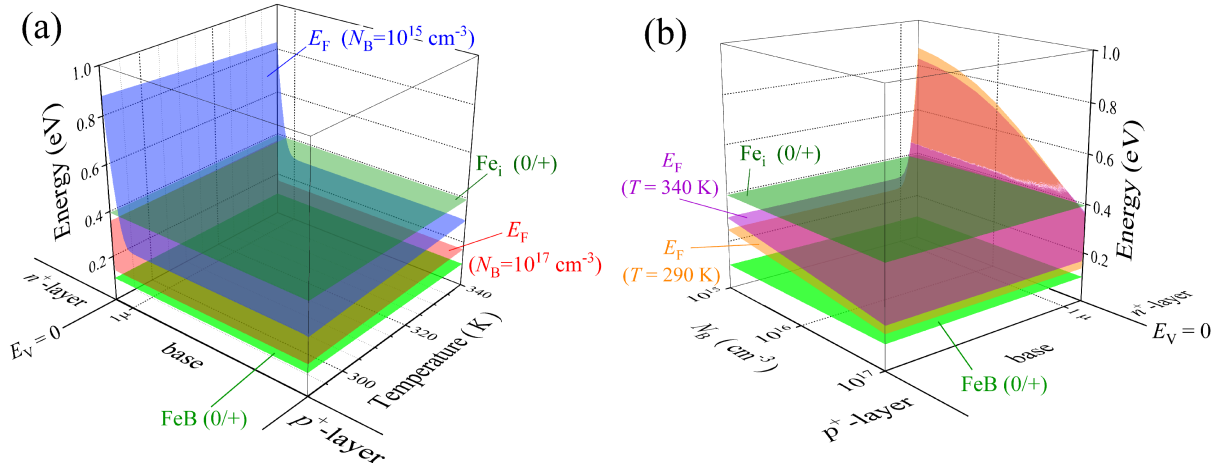


Figure 4: The location of the Fermi level in the base of the $n^+ - p - p^+$ structure as a function of temperature for $N_B = 10^{15}$ and 10^{17} cm^{-3} (a), and as a function of the doping level for $T = 290$ and 340 K (b). The zero energy value corresponds to the top of the valence band. Also shown are the positions of the donor levels of the FeB pair (green surfaces) and the interstitial iron atom Fe_i (olive surfaces).

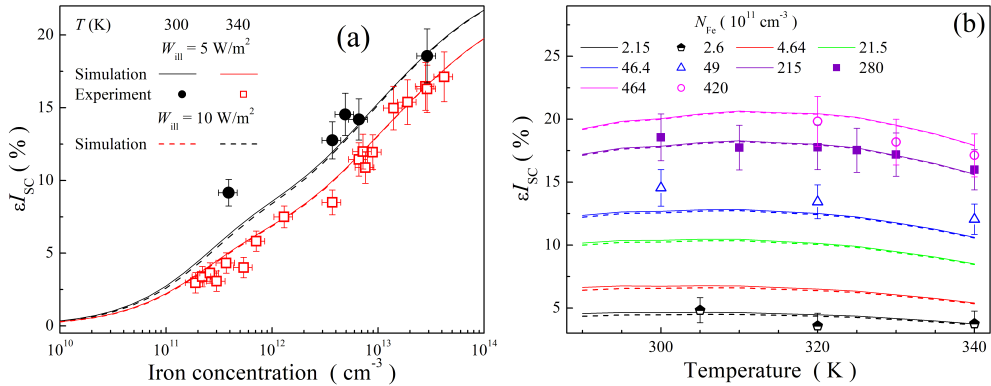


Figure 5: Dependencies of relative changes of short-circuit current on iron concentration (a) and temperature (b) for SSC with $d_p = 380 \mu\text{m}$ and $N_B = 1.36 \times 10^{15} \text{ cm}^{-3}$ in the case of monochromatic (940 nm) illumination. The marks are the experimental results (divided by factor 1.4), the lines are the simulation results. W_{ill} , Wm^{-2} : 5 (marks and solid lines), 10 (dotted lines). Different lines and marks correspond to different temperatures (a) or N_{Fe} values (b) — see legends.

3.2. Open-circuit voltage

3.3. Fill factor

3.4. Solar Cell Efficiency

4. Conclusion

References

- [1] B. P. Singh, S. K. Goyal, S. S. A., Grid connected-photovoltaic system (gc-pvs): Issues and challenges, IOP Conference Series: Materials Science and Engineering 594 (2019) 012032.
- [2] R. Basnet, D. Yan, D. Kang, M. M. Shehata, P. Phang, T. Truong, J. Bullock, H. Shen, D. Macdonald, Current status and challenges for hole-selective poly-silicon based passivating contacts, Appl. Phys. Rev. 11 (2024) 011311.
- [3] L. Wang, J. Liu, Y. Li, G. Wei, Q. Li, Z. Fan, H. Liu, Y. An, C. Liu, J. Li, Y. Fu, Q. Liu, D. He, Dislocations in crystalline silicon solar cells, Advanced Energy and Sustainability Research 5 (2024) 2300240.
- [4] C. Claeys, E. Simoen, Metal Impurities in Silicon- and Germanium-Based Technologies: Origin, Characterization, Control, and Device Impact, volume 270 of *Springer Series in Materials Science*, Springer International Publishing, Berlin/New York, 2018.
- [5] A. Goetzberger, W. Shockley, Metal Precipitates in Silicon p-n Junctions, J. Appl. Phys. 31 (1960) 1821–1824.

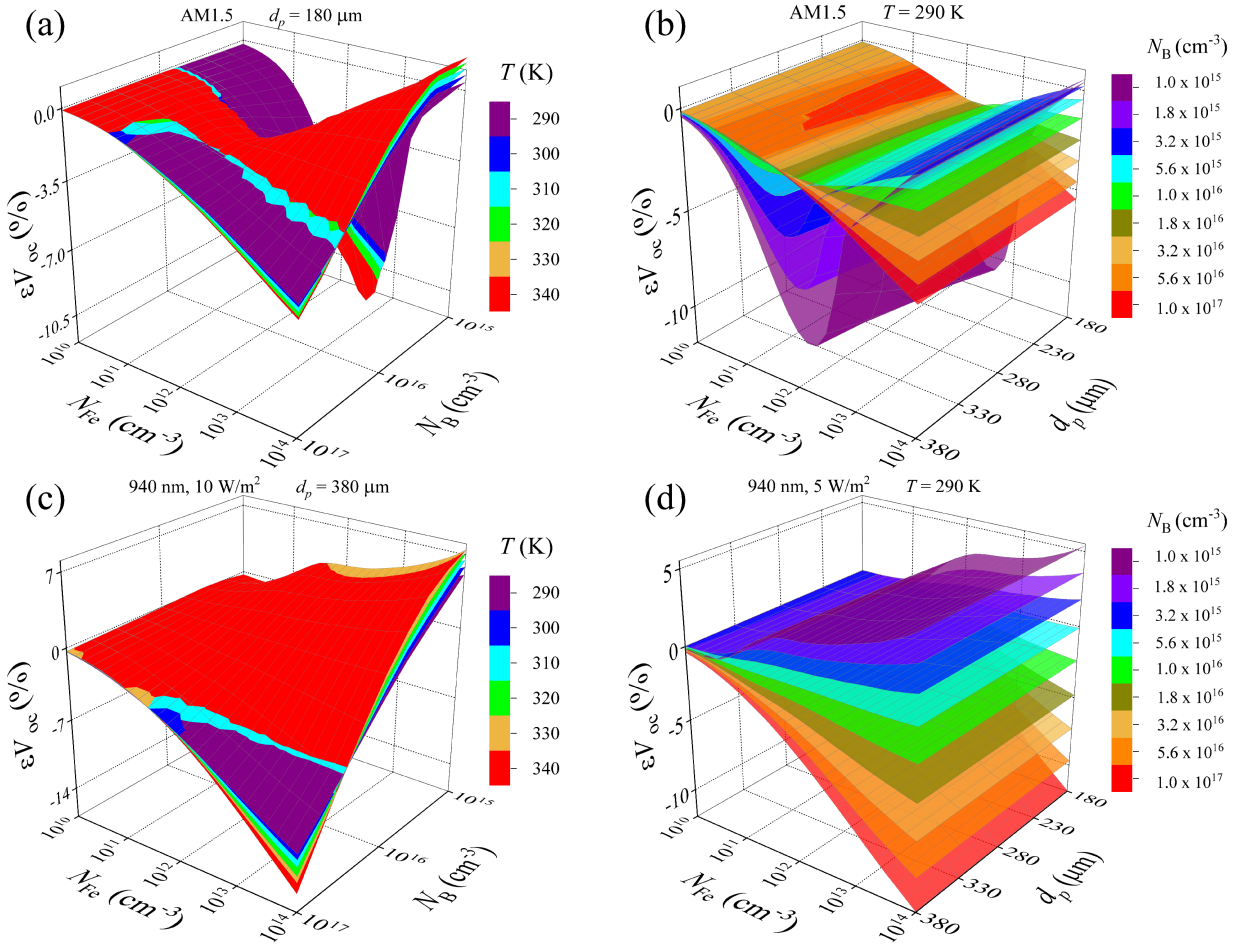


Figure 6: Dependencies of relative changes of open-circuit voltage on iron concentration and doping level (panels a and c) or base depth (b, d). Illumination: AM1.5 (a, b), 940 nm 10 Wm^{-2} (c), 940 nm 5 Wm^{-2} (d). T , K: 290 (b, d). Different surfaces correspond to different temperatures (a, c) and doping level (b, d).

- [6] O. Breitenstein, J. P. Rakotoniaina, M. H. Al Rifai, M. Werner, Shunt types in crystalline silicon solar cells, *Prog. Photovolt.: Res. Appl.* 12 (2004) 529–538.
- [7] K. Lee, A. Nussbaum, The influences of traps on the generation-recombination current in silicon diodes, *Solid-State Electron.* 23 (1980) 655–660.
- [8] A. A. Istratov, H. Hieslmair, E. Weber, Iron contamination in silicon technology, *Appl. Phys. A* 70 (2000) 489–534.
- [9] C. W. Pearce, R. G. McMahon, Role of metallic contamination in the formation of "saucer" pit defects in epitaxial silicon, *J. Vac. Sci. Technol.* 14 (1977) 40–43.
- [10] A. Hajjiah, M. Soha, I. Gordon, J. Poortmans, J. John, The impact of interstitial Fe contamination on n-type cz-silicon for high efficiency solar cells, *Sol. Energ. Mat. Sol.* 211 (2020) 110550.
- [11] T. T. Le, Z. Zhou, A. Chen, Z. Yang, F. Rougieux, D. Macdonald, A. Liu, Reassessing iron–gallium recombination activity in silicon, *J. Appl. Phys.* 135 (2024) 133107.
- [12] M. Maoudj, D. Bouhafs, N. E. Bourouba, A. Hamida-Ferhat, A. El Amrani, Study of the electrical properties of < 100 > cz p-type solar-grade silicon wafers against the high-temperature processes, *Appl. Phys. A* 127 (2021) 407.
- [13] O. Olikh, O. Datsenko, S. Kondratenko, Influence of illumination spectrum on dissociation kinetics of iron–boron pairs in silicon, *Phys. Status Solidi A n/a* (2024) 2400351.
- [14] H. S. Laine, V. Vähänissi, A. E. Morishige, J. Hofstetter, A. Haarhiltunen, B. Lai, H. Savin, D. P. Fenning, Impact of iron precipitation on phosphorus-implanted silicon solar cells, *IEEE Journal of Photovoltaics* 6 (2016) 1094–1102.
- [15] T. Buonassisi, A. A. Istratov, M. D. Pickett, M. Heuer, J. P. Kalejs, G. Hahn, M. A. Marcus, B. Lai, Z. Cai, S. M. Heald, Chemical natures and distributions of metal impurities in multicrystalline silicon materials, *Prog. Photovolt.: Res. Appl.* 14 (2006) 513–531.
- [16] M. Schubert, M. Padilla, B. Michl, L. Mundt, J. Giesecke, J. Hohl-Ebinger, J. Benick, W. Warta, M. Tajima, A. Ogura, Iron related solar cell instability: Imaging analysis and impact on cell performance, *Sol. Energy Mater. Sol. Cells* 138 (2015) 96–101.

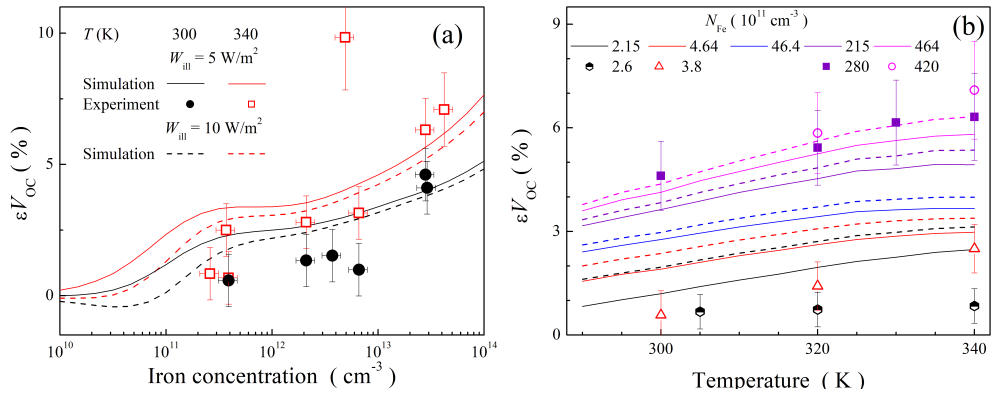


Figure 7: Dependencies of relative changes of open-circuit voltage on iron concentration (a) and temperature (b) for SSC with $d_p = 380 \mu\text{m}$ and $N_B = 1.36 \times 10^{15} \text{ cm}^{-3}$ in the case of monochromatic (940 nm) illumination. The marks are the experimental results, the lines are the simulation results. W_{ill} , Wm^{-2} : 5 (marks and solid lines), 10 (dotted lines). Different lines and marks correspond to different temperatures (a) or N_{Fe} values (b) — see legends.

- [17] A. Herguth, Quantification of iron in boron-doped silicon solar cells from open circuit voltage measurements, *IEEE J. Photovolt.* 12 (2022) 937–947.
- [18] L. Kimerling, J. Benton, Electronically controlled reactions of interstitial iron in silicon, *Physica B+C* 116 (1983) 297–300.
- [19] C. Möller, T. Bartel, F. Gibaja, K. Lauer, Iron-boron pairing kinetics in illuminated p-type and in boron/phosphorus co-doped n-type silicon, *J. Appl. Phys.* 116 (2014) 024503.
- [20] G. Zoth, W. Bergholz, A fast, preparation-free method to detect iron in silicon, *J. Appl. Phys.* 67 (1990) 6764–6771.
- [21] J. Toušek, J. Toušková, A novel approach to the surface photovoltage method, *Sol. Energy Mater. Sol. Cells* 92 (2008) 1020–1024.
- [22] S. Rein, S. W. Glunz, Electronic properties of interstitial iron and iron-boron pairs determined by means of advanced lifetime spectroscopy, *J. Appl. Phys.* 98 (2005) 113711.
- [23] J. Schmidt, D. Macdonald, Recombination activity of iron-gallium and iron-indium pairs in silicon, *J. Appl. Phys.* 97 (2005) 113712.
- [24] M. Goodarzi, R. A. Sinton, H. Jin, P. Zheng, W. Chen, Q. Wang, D. Macdonald, Accuracy of interstitial iron measurements on p-type multicrystalline silicon blocks by quasi-steady-state photoconductance, *IEEE J. Photovolt.* 7 (2017) 1216–1223.
- [25] O. Olikh, V. Kostilyov, V. Vlasuk, R. Korkishko, Y. Olikh, R. Chupryna, Features of FeB pair light-induced dissociation and repair in silicon n+-p-p+ structures under ultrasound loading, *J. Appl. Phys.* 130 (2021) 235703.
- [26] S. Herlufsen, D. Macdonald, K. Bothe, J. Schmidt, Imaging of the interstitial iron concentration in crystalline silicon by measuring the dissociation rate of iron–boron pairs, *Phys. Status Solidi RRL* 6 (2012) 1–3.
- [27] O. Olikh, Relationship between the ideality factor and the iron concentration in silicon solar cells, *Superlattices Microstruct.* 136 (2019) 106309.
- [28] O. Olikh, O. Lozitsky, O. Zavhorodnii, Estimation for iron contamination in si solar cell by ideality factor: Deep neural network approach, *Prog. Photovoltaics Res. Appl.* 30 (2022) 648–660.
- [29] J. Schmidt, Effect of dissociation of iron–boron pairs in crystalline silicon on solar cell properties, *Progress in Photovoltaics: Research and Applications* 13 (2005) 325–331.
- [30] D. H. Macdonald, L. J. Geerligs, A. Azzizi, Iron detection in crystalline silicon by carrier lifetime measurements for arbitrary injection and doping, *J. Appl. Phys.* 95 (2004) 1021–1028.
- [31] M. A. Green, Improved silicon optical parameters at 25°C, 295 K and 300 K including temperature coefficients, *Prog. Photovoltaics Res. Appl.* 30 (2022) 164–179.
- [32] T. Niewelt, B. Steinhauser, A. Richter, B. Veith-Wolf, A. Fell, B. Hammann, N. Grant, L. Black, J. Tan, A. Youssef, J. Murphy, J. Schmidt, M. Schubert, S. Glunz, Reassessment of the intrinsic bulk recombination in crystalline silicon, *Sol. Energ. Mat. Sol.* 235 (2022) 111467.
- [33] L. E. Black, D. H. Macdonald, On the quantification of auger recombination in crystalline silicon, *Sol. Energ. Mat. Sol.* 234 (2022) 111428.
- [34] A. Fell, K. R. McIntosh, P. P. Altermatt, G. J. M. Janssen, R. Stangl, A. Ho-Baillie, H. Steinkemper, J. Greulich, M. Müller, B. Min, K. C. Fong, M. Hermle, I. G. Romijn, M. D. Abbott, Input parameters for the simulation of silicon solar cells in 2014, *IEEE J. Photovolt.* 5 (2015) 1250–1263.
- [35] M. Burgelman, P. Nollet, S. Degraeve, Modelling polycrystalline semiconductor solar cells, *Thin Solid Films* 361–362 (2000) 527–532.
- [36] T. K. Joshi, G. Sharma, Y. R. Sharma, A. S. Verma, Spectroscopic screening and performance parameters of hybrid perovskite (ch3ch2ph3pb3) using wien2k and scaps-1d, *Phys. B Condens. Matter* 682 (2024) 415793.
- [37] B. K. Ravidas, A. Das, S. K. Agnihotri, R. Pandey, J. Madan, M. K. Hossain, M. K. Roy, D. Samajdar, Design principles of crystalline silicon/csgel3 perovskite tandem solar cells using a combination of density functional theory and scaps-1d frameworks, *Sol. Energ. Mat. Sol.* 267 (2024) 112688.
- [38] H. Liu, L. Xiang, Q. Liu, P. Gao, Y. Zhang, S. Li, F. Gao, Toward high-performance htl-free all-perovskite tandem solar cells: Scaps simulation, *IEEE J. Photovolt.* 14 (2024) 59–64.

- [39] L. You, X. Zhang, Q. Ma, W. Zhu, J. Wu, Optimization of electron transport layer-free $\text{Cs}_2\text{TiBr}_6/\text{MASnBr}_3$ laminated structure perovskite solar cells by scaps-1d simulation, *Phys. Status Solidi A* 220 (2023) 2300071.
- [40] A. Ait Abdelkadir, M. Sahal, Theoretical development of the czts thin-film solar cell by scaps-1d software based on experimental work, *Materials Science and Engineering: B* 296 (2023) 116710.
- [41] J. Liang, Y. Wang, Y. Zhang, X. Liu, J. Lin, Construction of perovskite homojunction for highly efficient perovskite solar cells by scaps-1d, *Materials Science and Engineering: B* 301 (2024) 117196.
- [42] M. Abdulmalik, E. Danladi, Influence of perovskite thickness on the performance of silver-doped NaZnBr_3 perovskite solar cells using scaps software, *Semiconductor Physics, Quantum Electronics & Optoelectronics* 26 (2023) 321–331.
- [43] R. Pässler, Dispersion-related description of temperature dependencies of band gaps in semiconductors, *Phys. Rev. B* 66 (2002) 085201.
- [44] D. Yan, A. Cuevas, Empirical determination of the energy band gap narrowing in p^+ silicon heavily doped with boron, *J. Appl. Phys.* 116 (2014) 194505.
- [45] R. Couderc, M. Amara, M. Lemiti, Reassessment of the intrinsic carrier density temperature dependence in crystalline silicon, *J. Appl. Phys.* 115 (2014) 093705.
- [46] M. A. Green, Intrinsic concentration, effective densities of states, and effective mass in silicon, *J. Appl. Phys.* 67 (1990) 2944–2954.
- [47] W. O'Mara, R. Herring, L. Hant, Handbook of semiconductor silicon technology, Noyes Publications, New Jersey, USA, 1990.
- [48] D. Klaassen, A unified mobility model for device simulation — I. model equations and concentration dependence, *Solid-State Electron.* 35 (1992) 953–959.
- [49] P. P. Altermatt, J. Schmidt, G. Heiser, A. G. Aberle, Assessment and parameterisation of Coulomb-enhanced Auger recombination coefficients in lowly injected crystalline silicon, *J. Appl. Phys.* 82 (1997) 4938–4944.
- [50] W. Wijaranakula, The reaction kinetics of iron–boron pair formation and dissociation in p -type silicon, *J. Electrochem. Soc.* 140 (1993) 275–281.
- [51] J. D. Murphy, K. Bothe, M. Olmo, V. V. Voronkov, R. J. Falster, The effect of oxide precipitates on minority carrier lifetime in p -type silicon, *J. Appl. Phys.* 110 (2011) 053713.
- [52] F. E. Rougieux, C. Sun, D. Macdonald, Determining the charge states and capture mechanisms of defects in silicon through accurate recombination analyses: A review, *Sol. Energy Mater. Sol. Cells* 187 (2018) 263 – 272.
- [53] A. A. Istratov, H. Hieslmair, E. Weber, Iron and its complexes in silicon, *Applied Physics A: Materials Science & Processing* 69 (1999) 13–44.
- [54] O. Olikh, V. Kostylyov, V. Vlasiuk, R. Korkishko, R. Chupryna, Intensification of iron–boron complex association in silicon solar cells under acoustic wave action, *J. Mater. Sci.: Mater. Electron.* 33 (2022) 13133–13142.
- [55] D. Yang (Ed.), Handbook of Photovoltaic Silicon, Springer Berlin, Heidelberg, first edition, 2019.
- [56] A. Goetzberger, J. Knobloch, B. Voss, Crystalline Silicon Solar Cells, Wiley, 1998.